Programmable Photonic Neural Networks

Angelina Totovic[1,*], George Giamougiannis[1], Apostolos Tsakyridis[1], David Lazovsky[2], and Nikos Pleros[1]

[1]Wireless and Photonics Systems and Networks (WinPhos) Research Group, Center for Interdisciplinary Research and Innovation - CIRI, Aristotle University of Thessaloniki, Balkan Center - Building A, 10th Km Thessalonikis-Thermis Av, 57001, Thessaloniki, Greece
[2]Celestial AI, 100 Mathilda Pl. Suite 170, Sunnyvale, CA 94086, USA
[*]angelina@auth.gr

ABSTRACT

Neuromorphic photonics has relied so far either solely on coherent or Wavelength-Division-Multiplexing (WDM) designs for enabling dot-product or vector-by-matrix multiplication, which has led to an impressive variety of architectures. Here, we go a step further and employ WDM for enriching the layout with parallelization capabilities across fan-in and/or weighting stages instead of serving the computational purpose and present, for the first time, a neuron architecture that combines coherent optics with WDM towards a multifunctional programmable neural network platform. Our reconfigurable platform accommodates four different operational modes over the same photonic hardware, supporting multi-layer, convolutional, fully-connected and power-saving layers. We validate mathematically the successful performance along all four operational modes, taking into account crosstalk, channel spacing and spectral dependence of the critical optical elements, concluding to a reliable operation with MAC relative error $< 2\%$.

Introduction

The explosive growth of Artificial Intelligence (AI) and Deep Learning (DL) together with maturing photonic integration have created a new window of opportunity for use of optics in computational tasks[1–5]. The use of photons and relevant optical technologies in Neural Network (NN) hardware is predicted to offer a significant boost in Multiply-Accumulate (MAC) operations per second compared to the respective NN electronic platforms, with computational energy and area efficiency being estimated to reach $<$ fJ/MAC and $>$ TMAC/sec/mm^2, respectively[6,7]. The pathway towards realizing this NN hardware paradigm-shift aims to exploit the high line-rates supported by integrated photonic technologies together with the small-size and low-power weighting function that can be offered at chip-scale[4,8]. So far, the vast majority of photonic devices utilized for weighting purposes has emphasized on slowly reconfigurable elements, like Thermo-Optic (T/O) phase shifters[9,10] and Phase-Change Material (PCM)-based non-volatile memory structures[4,8], implying that inference applications are currently considered as the main target within the area of neuromorphic photonics[3].

Inference engines indeed require a rather static neuron architecture and a layer connectivity graph that usually gets defined for optimally performing a certain AI task. Object tracking and image classification, for example, are typically performed via a number of convolutional layers followed by one or more Fully Connected (FC) layers, while autoencoders require cascaded stages of FC layers[11,12]. Although convolutional and FC layers comprise critical architectural elements in almost all inference platforms, a large set of parameters - such as the number of layers and/or neurons per layer and the connectivity graph - can vary significantly depending on the targeted DL architecture and application. Electronic implementations may conclude to Application-Specific Integrated Circuits (ASICs) customized for a specific inference task, but the use of GPUs, TPUs or even FPGAs becomes unavoidable when reprogrammability and reconfigurability are required in order to utilize the same hardware for multiple applications[13].

Transferring the reconfiguration capability to Photonic (P)-NN implementations requires a platform that can flexibly support different functional layouts over the same neural hardware. Programmability in photonics has made significant progress over the last years[14–16] and programmable Photonic Integrated Circuits (PICs) have been shown to offer important advantages towards releasing cost-efficient, flexible and multi-functional photonic platforms that can closely follow the concept of electronic FPGAs[17]. In this effort, it has also been highlighted that just the use of slowly reconfigurable 2×2 Mach-Zehnder Interferometric (MZI) switches within an appropriate architectural scheme can yield a large set of circuit connectivities and functionality options[14,15]. However, the idiosyncrasy of NN architectures has to proceed along alternative functionalities that are currently still not offered by programmable photonic implementations. Although weight value reconfiguration can be indeed offered by state-of-the-art photonic weighting technology[4,8–10] and a shift in perspective towards programmable activation functions has also started to emerge[16,18,19], neuromorphic photonic architectures demonstrated so far are not supporting any
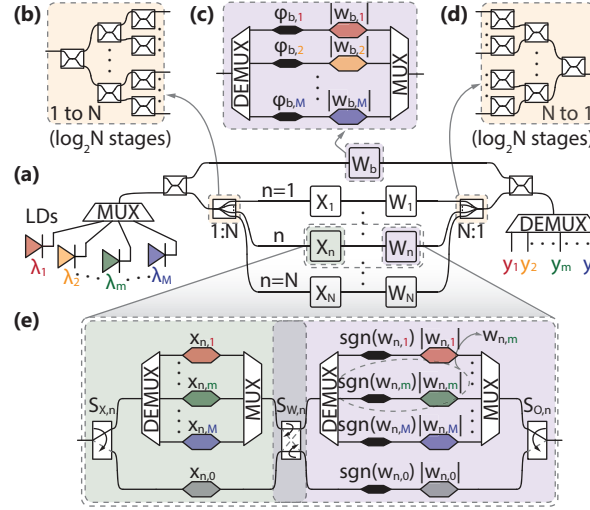
Figure 1. (a) Schematic representation of PPNN showing M laser diodes (LDs), a MUX, a 3dB X-splitter followed by a bias branch (W_b) and a reconfigurable OLAU encompassing 1-to-N splitting stage, input (X_n) and weight (W_n) modulator banks and an N-to-1 combiner stage, the output of which is brought to interfere with the bias signal within 3dB X-coupler and sent to the DEMUX. Closer look into (b) 1-to-N splitting and (d) its π-rotated N-to-1 coupling stage. Zoom-in into the (c) bias branch wavelength selective weights and phase modulators and (e) an axon of the OLAU consisting of switches for signal routing and modulators for inputs ($x_{n,m}$) and weights ($w_{n,m}$).

reconfiguration mechanism for their linear neuron stages. PNNs have so far progressed along two main architectural categories for realizing linear neural layers, where Wavelength-Division-Multiplexed (WDM) and coherent platforms seem to follow discrete and parallel roadmaps: *(i)* incoherent or WDM-based layouts, where a discrete wavelength is used for each axon within the same neuron[3,4,20], and *(ii)* coherent interferometric schemes, where a single wavelength is utilized across the entire neuron, exploiting interference between coherent electrical fields for weighted sum operations[9,10].

Here, we present a novel architecture that can efficiently combine WDM and coherent photonics towards supporting Programmable PNNs (PPNNs) with four different linear neural layer operational modes. Starting from our recently proposed dual-IQ coherent linear neuron architecture[21], that has been recently demonstrated also as a PIC with the ground breaking compute-rates per axon[22,23], we extend single neuron architecture by employing multiple wavelength channels and respective WDM De/Multiplexing (DE/MUX) structures towards creating multi- and single-element fan-in (input) and weight stages per every axon. Programmability is then enforced through 2×2 MZI switches that can flexibly define the connectivity between fan-in and weighting stages, allowing in this way for software-defined neural layer topologies. We formulate the mathematical framework for this programmable neuromorphic architecture and proceed with an in-depth study of the anticipated performance impairments originating from the use of multiple wavelengths within the same interferometric arrangement. We conclude to a simple mechanism for counteracting wavelength-dependent behaviour of modulators and phase shifters at the fan-in and weighting stage, respectively, showing that our programmable layout performs equally well for any number of employed optical channels in any of the 4 distinct modes of operation, with all supported neurons always offering a relative error lower than 2% as long as the inter-channel crosstalk is kept at typical values of less than $-20\,$dB.

PPNN architecture and operating principle

In our recent study[21] we have demonstrated how coherent linear neurons, offering dot-product functionality, can be constructed of IQ-modulator blocks, allowing for the sign information (encoded into the signal's phase) to be preserved by introducing the biasing signal, $\Sigma w_i x_i + b$, making the neuron compatible with all-optical nonlinear activation functions, $f_{NL}(\cdot)$, tailored either for electric field, or for optical power, without suffering information loss. Having the wavelength domain unexploited, we advance our original neuron architecture in order to accommodate multiple channels and achieve parallelization as shown in Fig. 1.

As Fig. 1(a) reveals, the backbone of our neural layer remains similar as in[21] with the main differences being: *(i)* a single Continuous Wave (CW) input optical signal is now replaced by M multiplexed CW signals, each centered at λ_m and supporting one independent virtual neuron, and *(ii)* input and weight modulators are now replaced by more elaborate modulator banks given in Fig. 1(c), (e), delimited by software-controllable switches in the case of latter. The input, multichannel signal is first
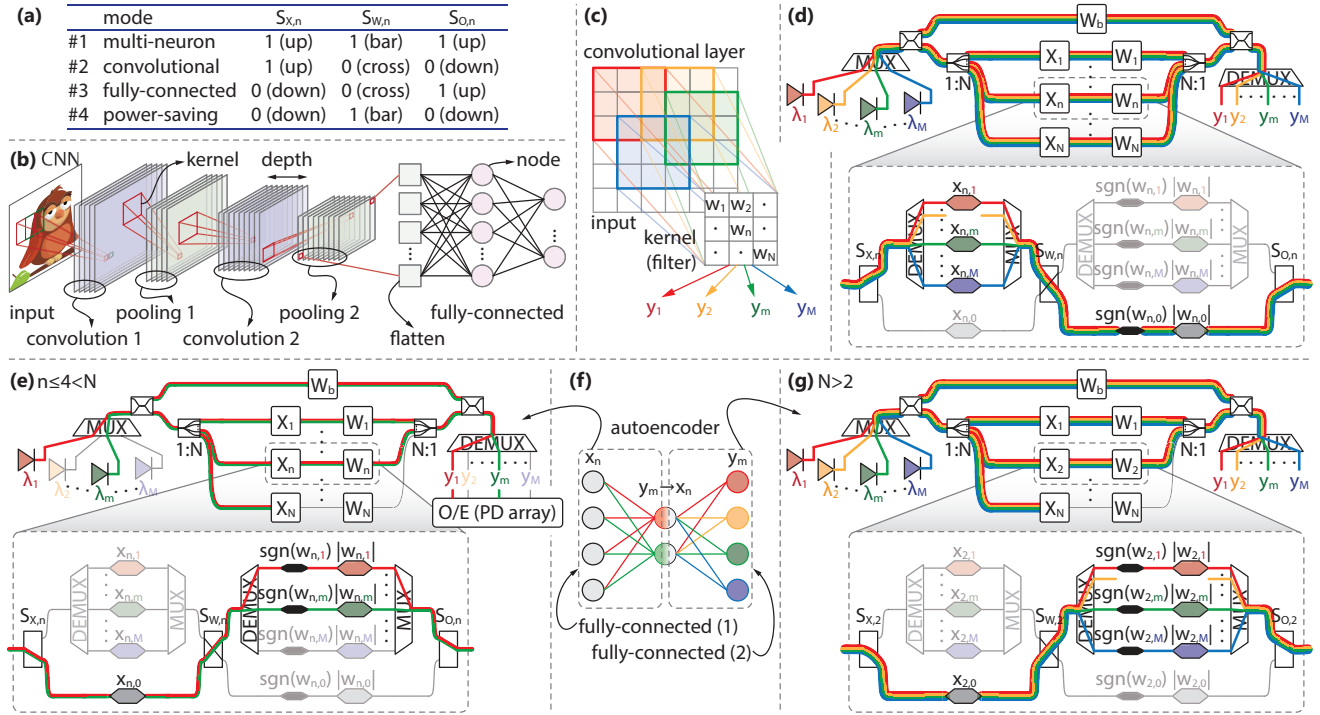
Figure 2. (a) PPNN modes of operation and the corresponding switch states. (b) Simplified CNN inspired by LeNet-5, employed in image classification. (c) Schematic of a convolutional layer with color coded input/output pairs and (d) its implementation over PPNN in mode #2 where each channel m corresponds to one input/output pair. (f) Schematic of an autoencoder and (e), (g) its two FC layers implemented over PPNN in mode #3 where channels correspond to unique weight vectors and outputs y_m.

split by a 3dB X-coupler to the portion directed to the bias branch and the remaining one entering the Optical Linear Algebraic Unit (OLAU). Within the OLAU, the signal gets further split equally in terms of power by a 1-to-N splitter, an example of which is given in Fig. 1(b), and, after being appropriately modulated by inputs $x_{n,m}$ and pondered by weights $w_{n,m}$, gets sent to the N-to-1 combiner, shown in Fig. 1(d). At this stage, the output signal interferes with the bias within a 3dB X-coupler and is forwarded to the DEMUX to generate the outputs y_m. Finally, each channel m will have its own algebraic addition of the weighted inputs with a designated bias, concluding to a total of M independent N-fan-in neurons.

Depending on the configuration of switches, an overview of which is given in Fig. 2(a), channels within a single axon from Fig. 1(e), can be controlled either individually or by a common modulator, allowing the network to operate as:

1. *multi-neuron* (M independent N-to-1 neurons), allowing for an arbitrary logical interconnection graph, supporting even a multi-layer operation by designating different neurons to different layers of the NN;
2. *convolutional* (M independent N-element inputs with a single kernel of size N), where all different input vectors pass through the same set of weights, Fig. 2(d), achieving simultaneous M-fold usage of the same kernel, speeding up convolution operation from Fig. 2(c);
3. *fully-connected* (FC) (single N-element input over M neurons), where a single input passes through all M available weight sets, each of size N, allowing for full connectivity between all inputs and outputs, Fig. 2(e), (g);
4. *power-saving* (single N-to-1 neuron), which allows for resource conservation by powering-off the excess channels and is particularly useful for the NNs operating in sequential manner (one neuron at a time).

A detailed mapping between the architecture from Fig. 1 and the enlisted modes of operation can be found in Section 1, Supplementary Document, with some examples also given in Fig. 2. Convolutional and FC modes of operation are particularly important due to their ubiquitous presence in deep NNs, especially in the widely-used Convolutional NNs (CNNs), Fig. 2(b)[11]. In both convolutional and pooling layers, a unique kernel (filtering or weighting window) is applied to the inputs in a scanning manner with a certain stride, yielding a single output value, as depicted schematically in Fig. 2(c) and implemented over PPNN in Fig. 2(d). On the other hand, FC layer, shown implemented over PPNN in Fig. 2(e), (f), has a single set of inputs passing through multiple sets of weights to produce the outputs and it is the main building block of autoencoders, Fig. 2(f), along with being necessary in CNNs, Fig. 2(b). Both of these operations are time and energy consuming if approached to in a sequential

Table 1. Input and weight matrices of the n-th axon

mode	X_n	W_n
#1	$\mathrm{diag}[x_{n,1},\ldots,x_{n,M}]$	$\mathrm{diag}[w_{n,1},\ldots,w_{n,M}]$
#2	$\mathrm{diag}[x_{n,1},\ldots,x_{n,M}]$	$w_{n,0}I_M$
#3	$x_{n,0}I_M$	$\mathrm{diag}[w_{n,1},\ldots,w_{n,M}]$
#4	$x_{n,0}I_M$	$w_{n,0}I_M$

manner, implying that they greatly benefit from parallelization.

Although the switches of different axons can be controlled independently, the resulting mixed type NN layer has no application foreseen at the moment. Therefore, we assume that switches in all branches are synchronized in the following manner $S_{X,n} = S_X$, $S_{W,n} = S_W$ and $S_{O,n} = S_O, \forall n$. The matrices encapsulating the values of the inputs, X_n, and weights, W_n, for different modes of operation are summarized in Table 1 where I_M stands for $M \times M$ identity matrix. Inputs require no more than one amplitude modulator per value, since they are defined on the positive domain $x_{n,m} \in [0,1]$, whereas, in case of weights, which can be both positive and negative, $w_{n,m} \in [-1,1]$, two modulators are required, one for the amplitude, which will be proportional to the weight magnitude, $|w_{n,m}|$, and the remaining for the phase, which will be carrying the sign of the weight, $\varphi_{n,m} = [1 - \mathrm{sgn}(w_{n,m})]\pi/2$.

The bias branch, given in Fig. 1(c) differs from the axon branch, Fig. 1(e), in two aspects: (*i*) it has no input sequence modulator(s); (*ii*) it has only one possible route the signal can take, with a separate control of each channels' phase and amplitude. The latter comes as a counteraction measure to the anticipated wavelength-dependent variation of the weight magnitudes when a single phase- and amplitude-modulator is used in each axon of the OLAU and it also allows for compensating potentially different phase offsets that will be accumulated by different channels within OLAU, therefore meeting the conditions for constructive interference in the last 3dB coupler of the PNN. Bias matrix remains the same for all modes of operation and reads $W_b = \mathrm{diag}[w_{b,1},\ldots,w_{b,M}]$, where $w_{b,m} = |w_{b,m}|\exp(i\varphi_{b,m})$.

Let us assume that the optical carrier consists of M channels λ_m, and is represented via an $M \times 1$ column-vector of electric fields $\mathrm{E_{LD}} = [E_{LD,1},\ldots,E_{LD,M}]^T$, which are normalized such that their magnitude squared yields optical power, i.e., $E_{LD,m} = \sqrt{P_{LD,m}}\exp(i\varphi_{LD,m})$. Following the architecture given in Fig. 1 and the detailed derivation presented in Section 2 of Supplementary Document, we find the column-vector of electric fields at the output of PPNN as

$$\mathrm{E_{out}} = \frac{1}{2}\left(e^{i\pi/2}\right)^{1+\log_2 N}\left(\widetilde{W}_b + \frac{1}{N}\sum_{n=1}^{N} W_n X_n\right) \times \mathrm{E_{LD}}, \tag{1}$$

where, in order to ensure constructive interference at the last 3dB X-coupler of Fig. 1(a), phase matching between the bias and the signal coming from OLAU is performed. The former is done through $\widetilde{W}_b = W_b \exp(-i\pi/2)^{\log_2 N}$, which denotes the bias branch channel-wise transfer matrix accounting for phase alignment, with its m-th element being $\widetilde{w}_{b,m} = |w_{b,m}|\exp(i\varphi_{b,m})\exp(-i\pi/2)^{\log_2 N}$. Disregarding accumulated phase shift and losses that are identical for all channels, the transfer matrix of the PPNN, Q_t, can be written as

$$Q_t = \mathrm{diag}[q_{t,1},\ldots,q_{t,M}] = \widetilde{W}_b + \frac{1}{N}\sum_{n=1}^{N} W_n X_n, \tag{2a}$$

$$q_{t,m} = \widetilde{w}_{b,m} + \frac{1}{N}\sum_{n=1}^{N} w_{n,m}x_{n,m}. \tag{2b}$$

The m-th element of Q_t matrix, $q_{t,m}$, given by equation (2b) for multi-neuron mode of operation (#1), reveals the underlying principle of operation of our PPNN, demonstrating how normalized dot-product between the N-element vectors represented across axons, $[w_{1,m},\ldots,w_{N,m}]$ and $[x_{1,m},\ldots,x_{N,m}]$, can be achieved at the m-th channel neuron output with bias $\widetilde{w}_{b,m}$ superimposed to it. The reconfigurability of PPNN is concealed in equation (2a), where the choice of matrices X_n and W_n is governed by the mode of operation according to the Table 1, leading to alternative functionalities. In convolutional mode (#2), a single kernel as in Fig. 2(c), i.e., a single set of weights across different channels $[w_{1,0},\ldots,w_{N,0}]$, calls for common weight modulator per axon since $w_{n,m} = w_{n,0}, \forall m$, whereas the input vectors remain different across the channels, $[x_{1,m},\ldots,x_{N,m}]$, concluding to M-fold parallelization, and consequently acceleration, of convolution operation. On the other hand, in FC mode (#3), a single input vector $[x_{1,0},\ldots,x_{N,0}]$, calling for one input modulator $x_{n,0}$ per n-th axon, is passed through multiple, channel selective, weights, $[w_{1,m},\ldots,w_{N,m}]$, yielding full connectivity between all N inputs $x_{n,0}$ and all M outputs y_m, as depicted in Fig. 2(f). Finally, in power-saving mode (#4), unique weight and input vectors, $[w_{1,0},\ldots,w_{N,0}]$ and $[x_{1,0},\ldots,x_{N,0}]$, allow for only one

channel to be used and the remaining ones to be powered off, offering the same functionality as our dual-IQ dot-product engine from[21] without additional penalties in power consumption.

As noted earlier, equation (2b) is given for mode #1, but can be updated to any other by replacing the channel-specific $x_{n,m}$ and/or $w_{n,m}$, by a joint $x_{n,0}$ and/or $w_{n,0}$. In what follows, except when explicitly noted otherwise, we will be using $x_{n,m}$ and $w_{n,m}$ notation for an arbitrary mode of operation for simplicity and clarity.

In certain application scenarios, such as image classification, Fig. 2(b), (c), it is convenient to choose the number of axons as a square of the linear filter (kernel) dimension which is typically an odd number, resulting in, e.g., $N = 3 \times 3$ or $N = 5 \times 5$. Some other applications may call for an arbitrary N, not necessarily a square. In this case two approaches can be adopted to exploit the PPNN architecture from Fig. 1, bearing in mind that splitter and combiner from Fig. 1(b), (d) were engineered assuming N to be a power of 2. First approach is straight-forward and assumes using the N needed axons and ignoring the remaining ones that are supplementing to the closest power-of-2 number larger than N. In this case, certain amount of optical power will be lost, but being proportional to $N/2^{\lceil \log_2 N \rceil}$, loss will never exceed 3dB. Second approach aims to eliminate power losses at the expense of redesigning the splitter and combiner, asserting identical phase shift along all paths resulting in coherence preservation between the signals traveling along different axons. The algorithm for designing such splitter and the corresponding combiner is presented in Section 3 of Supplementary Document.

Impairment Analysis

Operating PPNN in power-saving mode with a single active channel, opens the possibility to bypass the DE/MUXes in axons and center each of the input and/or weight modulators' transfer function to the channel's central wavelength, leaving no room for output degradation due to wavelength dependent properties of optical components. On the other hand, having a multichannel PPNN (modes #1 through #3) rightfully raises a concern on whether all channels will perform in equal manner, having similar relative error between the targeted output, given by matrix element $q_{t,m}$ in equation (2b), and experimentally obtained value $q_{e,m}$. The wavelength dependent loss and phase accumulation along with the crosstalk in DE/MUXes could lead to performance degradation of some channels to a higher extent than the others, measured by increase of absolute, $\Delta q_m = q_{e,m} - q_{t,m}$, and relative error, $\delta q_m = |\Delta q_m|/q_{t,m}$, between the matrix elements. Setting the limit for tolerable relative error can be a challenging task as the network's error-tolerance depends on the assignment in which it is employed and on the training algorithm. As a rule of thumb, an acceptable PPNN error should be lower than the training error, which is commonly in the range of few percent[21–23]. Moreover, employing noise-aware training algorithms has proven to increase the resilience of the NN models even in the noisy environment[24], where the noise should be understood as a broad term encapsulating any randomly distributed deviation from the targeted output. Following the above said, in this Section we set to investigate how much will the experimental PPNN transfer matrix, Q_e, deviate from the targeted one, Q_t, and whether this deviation can be counteracted.

For implementing the inputs $x_{n,c}$, we use Mach-Zehnder Modulators (MZMs) in our study, with c being the index of the channel λ_c at which the MZM is centered. We assume that MZMs have voltage-controlled Phase Shifters (PS) in both arms (indexed as "1/2" for upper/lower arm, respectively) and are operated in push-pull configuration with DC induced phase shifts given as $\phi_{DC,1/2} = 2\pi n(V_{DC,1/2}, \lambda) L_{DC}/\lambda$ and RF induced as $\phi_{1/2}(\pm V_{RF}, \lambda) = \phi_0(\lambda) \pm \Delta\phi(V_{RF}, \lambda)$ with $\phi_0 = 2\pi n_0(\lambda) L/\lambda$ and $\Delta\phi = 2\pi \Delta n(V_{RF}, \lambda) L/\lambda$ where L and L_{DC} denote the lengths of RF and DC active regions and $n = n_0 + \Delta n$, with n_0 and Δn being the refractive index at zero applied voltage and its deviation when the voltage is applied. The transfer function of the MZM is given as

$$t_{MZM}(\lambda) = \cos\left\{\left[2\Delta\phi(\lambda) + \phi_{DC,1}(\lambda) - \phi_{DC,2}(\lambda)\right]/2\right\} \times \exp\left\{i\left[2\phi_0(\lambda) + \phi_{DC,1}(\lambda) + \phi_{DC,2}(\lambda)\right]/2\right\}, \tag{3}$$

and is tailored such that $t_{MZM}(\lambda_c) = x_{n,c}$ by choosing the DC voltages (biases) which induce phase shifts separated by π, implying $\phi_{DC,1} = \phi_{DC} - \pi$ and $\phi_{DC,2} = \phi_{DC}$. Assuming that the modulation-induced phase-variation does not contribute significantly to the overall wavelength dependence, the MZM transfer function can be approximated by

$$t_{MZM}(\lambda) \approx \sin\Delta\phi(\lambda_c) \exp\left\{i\left[\phi_0(\lambda) + \phi_{DC}(\lambda) - \frac{\pi}{2}\right]\right\}. \tag{4}$$

For modes of operation #3 and #4, MZM transfer function will be centered at a certain λ_c, i.e., optimized to deliver targeted input $x_{n,c}$ at the given channel by enforcing $\Delta\phi(V_{RF}, \lambda_c) = \arcsin x_{n,c}$ and setting the argument of the exponential function in equation (3) to a multiple of 2π. For any other channel m, the imprinted value $x_{n,m,c}$ will deviate from the targeted one. Following the detailed analysis of the input modulator operation given in Section 4 of Supplementary Document, relying on the 1st order Taylor expansion of the phases $\phi_0(\lambda)$ and $\phi_{DC}(\lambda)$ around λ_c, we find that the m-th channel of the n-th axon carries the

input value given by

$$x_{n,m,c} \approx x_{n,c} \exp\left(-i\xi_{m,c}^{(x)}\right), \tag{5a}$$

$$\xi_{m,c}^{(x)} = 2\left(p_x + q_x + \frac{1}{4}\right)\pi \frac{n_{\mathrm{g}}(\lambda_c)}{n(\lambda_c)}\frac{1}{\lambda_c}(m-c)\Delta\lambda_1, \tag{5b}$$

where $p_x = n_0(\lambda_c)L/\lambda_c$ and $q_x = n(V_{\mathrm{DC}},\lambda_c)L_{\mathrm{DC}}/\lambda_c$ stand for normalized lengths of the RF and DC phase shifters within the MZM and are restricted to $p_x, q_x \in \mathbb{N}$, n_{g} is the group refractive index, and $\Delta\lambda_1 = \lambda_{m+1} - \lambda_m$ denotes channel spacing (assuming equidistant channels). Parameter $\xi_{m,c}^{(x)}$ represents the phase shift accumulated by channel m and reveals four important facts: (*i*) it does not depend on targeted $x_{n,c}$ value implying that the phase accumulation does not vary with the input sequence; (*ii*) it does not depend on the axon index n, implying that all axons introduce the same amount of phase accumulation that can be compensated outside the OLAU rather than within the OLAU itself; (*iii*) it depends on the difference between m and c implying that all side channels of the same order have the same phase accumulation which magnitude increases with $|m-c|$; (*iv*) it increases with the channel spacing $\Delta\lambda_1$.

In order to implement the weights $w_{n,c}$ a combination of MZM and an independent PS can be used. Depending on targeted application, amplitude modulation can be achieved either through absorption control[4,8,23] or by employing interferometric modules[9,10,22] using either T/O or E/O PSs. Aligning with the majority of reported state-of-the-art coherent layouts targeting inference, and thus allowing slow reconfiguration rates, we choose thermally controlled PSs both within MZM's arms and in the PS that follows. Unlike E/O MZM, the T/O MZM cannot be operated in push-pull configuration; instead, it can be made asymmetrical by changing the length of the waveguide(s) in one or both of its arms to achieve a built-in phase difference of 2θ at the nominal temperature T_0 and λ_c, or, in other words, it will be biased at 2θ-point. At any point in time, only one PS is being used for adjusting the weight magnitude depending on the ratio of $|w_{n,c}|$ and $\cos\theta$. This is reflected in the electric field transfer function of the MZM-PS system

$$t_{\mathrm{MZM-PS}}(\lambda) = \cos\left[\theta - \mathrm{sgn}\left(|w_{n,c}| - \cos\theta\right)\Delta\phi(\Delta T,\lambda)/2\right] \times \exp\left\{i\left[\phi(T_0,\lambda) + \Delta\phi(\Delta T,\lambda)/2 + \phi_3(\lambda)\right]\right\}, \tag{6}$$

where $\phi(T_0,\lambda) = 2\pi n(T_0,\lambda)L/\lambda$ is the phase accumulated in MZM at T_0, $\Delta\phi(\Delta T,\lambda) = 2\pi\Delta n(\Delta T,\lambda)L/\lambda$ is the phase shift due to applied differential temperature ΔT, and $\phi_3(T,\lambda) = 2\pi n(T,\lambda)L_3/\lambda$ is the phase accumulated in the standalone PS. Similar to the case of input MZM, we can neglect the contribution of $\Delta\phi$ variation with the wavelength and approximate the MZM-PS transfer function by

$$t_{\mathrm{MZM-PS}}(\lambda) \approx |w_{n,c}| \times \exp\left\{i\left[\phi(T_0,\lambda) + \Delta\phi(\Delta T,\lambda_c)/2 + \phi_3(\lambda)\right]\right\}, \tag{7}$$

taking into account that it will be centered at λ_c yielding $t_{\mathrm{MZM-PS}}(\lambda_c) = w_{n,c}$, implying also $\phi(T_0,\lambda_c) = 2p_w\pi$ and

$$\Delta\phi(\Delta T,\lambda_c) = 2\,\mathrm{sgn}\left(|w_{n,c}| - \cos\theta\right)\left(\theta - \arccos|w_{n,c}|\right), \tag{8a}$$

$$\phi_3(\lambda_c) = \frac{1 - \mathrm{sgn}(w_{n,c})}{2}\pi + 2p_s\pi - \frac{1}{2}\Delta\phi(\Delta T,\lambda_c), \tag{8b}$$

where $p_w, p_s \in \mathbb{N}$. For any channel $m \neq c$, staying restricted to the 1$^{\text{st}}$ order approximation and assuming $p_w, p_s \gg 1$ which is expected in all cases of practical interest, following the detailed derivation given in Section 5 of Supplementary Document, we find that the m-th channel of the n-th axon carries the weight

$$w_{n,m,c} \approx w_{n,c}\exp\left(-i\xi_{m,c}^{(w)}\right), \tag{9a}$$

$$\xi_{m,c}^{(w)} = 2(p_w + p_s)\pi\frac{n_{\mathrm{g}}(\lambda_c)}{n(\lambda_c)}\frac{1}{\lambda_c}(m-c)\Delta\lambda_1, \tag{9b}$$

where $p_w = n(T_0,\lambda_c)L/\lambda_c$ and $p_s = n(T_0,\lambda_c)L_3/\lambda_c$ represent normalized lengths of the PSs within the MZM and the standalone PS, respectively, with L and L_3 being their lengths. Same conclusions enlisted earlier for $\xi_{m,c}^{(x)}$ hold for $\xi_{m,c}^{(w)}$.

For signal multiplexing and demultiplexing Arrayed Waveguide Gratings (AWGs) are used, with a flat channel-wise spectral response over the frequency band of interest. We assume that the AWG's power transfer function is given as a parabola in logarithmic domain, symmetrical and centered at the channel's wavelength, and that it introduces negligible overall losses. In linear domain, the transfer function corresponds to the far-field shape, i.e., a Gaussian function versus the wavelength[25]. The crosstalk of the AWG, defined as the ratio of powers of the first suppressed channel and the pass channel, is denoted as r_{AWG} in linear terms, or R_{AWG} in logarithmic (dB) domain. In what follows, we assume zero insertion loss and restrict ourselves to the

1st order approximation where it is assumed that the crosstalk is relevant only between adjacent channels. We also assume that the curvature of the output free-propagating region of the AWG matches the curvature of the Gaussian field (its equiphase line in transversal plane) yielding zero-phase difference between adjacent output waveguides.

When passing through the DEMUX, channel m will be distributed not only to the m-th output port, but also to ports $(m \pm 1)$, with the ratio of powers being determined by r_{AWG}. This will cause the m-th channel in adjacent waveguides to be modulated by input or weight targeted at channels $(m \pm 1)$. Subsequently, when collected by MUX, reversed process will follow, which will gather all the signals back to the output, leading to mixing of inputs or weights belonging to the three adjacent paths, with the appropriate coefficients. Following the detailed derivation given in Section 6 of Supplementary Document, we find that the actual, imprinted value of the input in modes of operation #1 and #2 deviates from the targeted one as

$$x_{n,m}^{\mathrm{AWG}} \approx x_{n,m} + r_{\mathrm{AWG}}\left(x_{n,m-1} - 2x_{n,m} + x_{n,m+1}\right), \tag{10}$$

under the constrain $x_{n,0} = x_{n,M+1} = 0$ and with the same formalism being applied to weights in modes #1 and #3, and biases in all modes of operation. Unlike the deviation coming from using a single modulator for multiple channels, which can be compensated to a certain extent, the crosstalk originating from the AWG cannot be easily counteracted outside the OLAU as it its pattern-dependent and, consequently, depends both on the index of the axon n and index of the channel m.

Having identified wavelength-dependent behaviour of the PPNN's constituent components, its experimental diagonal transfer matrix, Q_{e}, can be derived based on the PPNN configuration for different modes of operation, as per Fig. 2(a) and Table 1, following the path of the signal in Fig. 1(e), relying on equation (10) for modeling the AWG response, and equations (3) and (6) for unapproximated input and weight modulator transfer functions. Similar as in the case of Q_{t} in equation (2a), we disregard the accumulated phase shift in Q_{e} and restrain our focus only to the phase difference between the bias branch and the OLAU and between the axons in the OLAU itself, as these lead to potential performance deterioration through impairment of interference conditions. In order to perform phase alignment between the bias branch and the OLAU in modes of operation which assume using a single modulator for enforcing inputs or weights to multiple channels (mode #3 for inputs and #2 for weights), we modify the bias branch transfer matrix from $\widetilde{W}_{\mathrm{b}}$ to $\widetilde{W}_{\mathrm{b}}\Xi_c^{(w)}$ in mode #2 or $\widetilde{W}_{\mathrm{b}}\Xi_c^{(x)}$ in mode #3, where

$$\Xi_c^{(x/w)} = \mathrm{diag}\left[\exp\left(i\xi_{1,c}^{(x/w)}\right),\ldots,\exp\left(i\xi_{M,c}^{(x/w)}\right)\right], \tag{11}$$

with $\xi_{m,c}^{(x)}$ and $\xi_{m,c}^{(w)}$ being defined by equations (5b) and (9b), respectively. In this manner, channel-selective phase accumulation originating from equations (5a) and (9a) is cancelled, as detailed in Section 7 of Supplementary Document. It should be stressed that Q_{e} derived based on equations (5), (9) and (10) is approximate and, even though the phase compensation is carried out via the PSs in the bias branch, certain deviation from Q_{t} will remain. In the forthcoming analysis, these will be quantified by absolute, $\Delta q_m = q_{\mathrm{e},m} - q_{\mathrm{t},m}$, and relative error, $\delta q_m = |\Delta q_m|/q_{\mathrm{t},m}$, between the experimental, $q_{\mathrm{e},m}$, and targeted, $q_{\mathrm{t},m}$, diagonal matrix elements. The errors can be derived based on the expressions correlating $q_{\mathrm{e},m}$ and $q_{\mathrm{t},m}$ in Section 7 of Supplementary Document.

PPNN performance analysis

For our case-study, we assume silicon platform, with the refractive index dependence on wavelength at different temperatures taken from[26]. At $\lambda_c = 1.55\,\mu\mathrm{m}$ and $T_0 = 293\,\mathrm{K}$ we have $n = 3.4757$ and $n_{\mathrm{g}} = 3.5997$. In case of E/O modulators, unless doping is severe and/or composite materials are used, optical properties of the undoped silicon (where the majority of light is confined) remain the same as above, whereas the dependence of the refractive index on the voltage is assumed to be approximately linear for the voltage ranges of interest.

Using Monte-Carlo method, we observe 10^4 sets of random, uniformly distributed input and weight values, chosen on the domain $x_{n,m} \in [0,1]$ and $w_{n,m} \in [-1,1]$ and keep the bias fixed to $\widetilde{w}_{\mathrm{b},m} = 1$ in order to ensure that the information about the sign of the sum is preserved when transitioning to the power domain. When employing PPNN in trained environment, bias weight can take any value from $\widetilde{w}_{\mathrm{b},m} \in [-1,1]$ imposed by the training algorithm. Following the simulation, the diagonal matrix elements $q_{\mathrm{t},m}$ and $q_{\mathrm{e},m}$ are aggregated and 2-D scatter plots analyzed using multivariate statistical approach to determine deviations in terms of absolute and relative error.

Figure 3 shows 2-D scatter plots for two different modes of operation, convolutional (left-hand-side) and FC (right-hand-side), for T/O MZM biasing point $\theta = \pi/3$, normalized lengths $p_x = q_x = 100$ and $p_w = p_s = 50$, nominal channel spacing $\Delta\lambda_1 = 0.8\,\mathrm{nm}$, translating to approximately 100 GHz in frequency domain, and $R_{\mathrm{AWG}} = -15\,\mathrm{dB}$. Phase alignment between the bias branch and the OLAUs output has been carried out following equation (11).

In terms of magnitude of the experimental matrix element, $|q_{\mathrm{e},m}|$, versus the targeted matrix element, $q_{\mathrm{t},m}$, both modes of operation show similar performance, as confirmed by Fig. 3(a), (b), when optimized for the same channel, $c = 2$, out of $M = 4$ color-coded channels in the PPNN when a single modulator is used, or, optimized for m if a modulator per channel is used.
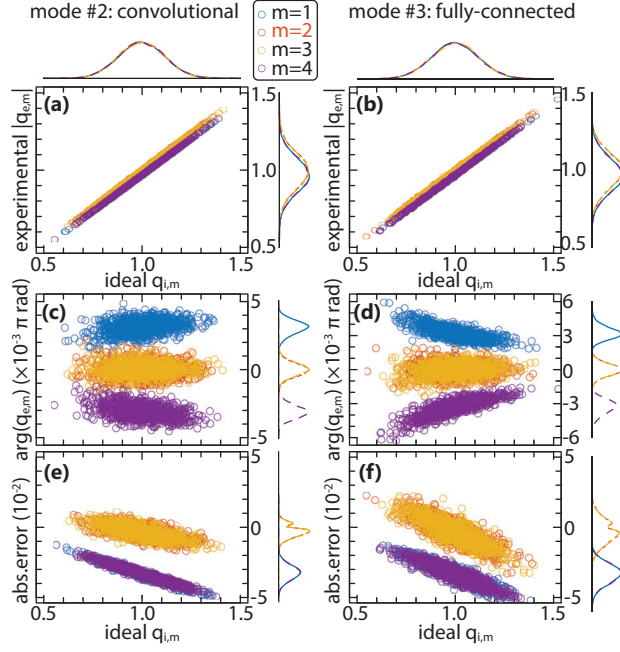
Figure 3. Comparison between the convolutional (#2, left-hand-side) and the fully-connected (#3, right-hand-side) mode of PPNN operation with $M = 4$ channels, optimized for operation at channel $c = 2$, and $N = 8$ axons for $\Delta\lambda_1 = 0.8$ nm and $R_{AWG} = -15$ dB. Channel-wise color coded 2-D scatter plots of the targeted matrix element $q_{t,m}$ and (a), (b) the magnitude and (c), (d) the argument of the experimental matrix element $|q_{e,m}|$ and (e), (f) the algebraic magnitude of the absolute deviation of the experimental from targeted matrix element, $\mathrm{sign}(\mathfrak{Re}\{\Delta q_m\})|\Delta q_m|$, with $\Delta q_m = q_{e,m} - q_{t,m}$, all with displayed univariate kernel probability density plots on the corresponding horizontal and vertical axes of the scatter plots.

The Spearman's rank correlation coefficient ρ in both cases given in Fig. 3(a), (b) exceeds 0.999 for all 4 observed channels, indicating almost perfect monotonic relation between the two quantities. The univariate Probability Density Functions (PDFs) of both $q_{t,m}$ and $|q_{e,m}|$ retain Gaussian shape, complying with Central Limit Theorem (CLT). Nevertheless, a slight downshift in the means of edge channels' PDFs can be observed ($m = 1$ and $m = 4$), were the side channels' optical power gets irreversibly lost during demultiplexing step, captured by $x_{n,0} = x_{n,M+1} = 0$ and $w_{n,0} = w_{n,M+1} = 0$ in equation (10) and its counterpart for $w_{n,m}^{AWG}$.

Scatter plots of the argument of $q_{e,m}$ versus $q_{t,m}$, given in Fig. 3(c), (d), reveal that phase alignment based on the approximate expression given by equations (5b) and (9b) yields excellent results, bringing the residual phase shifts below 0.01π rad. The distribution of $\arg(q_{e,m})$ is well approximated by Gaussian owing to CLT and depends to a certain extent on the targeted matrix element $q_{t,m}$ value. It can be also noticed that the edge channels ($m = 1$ and $m = 4$) suffer a shift of the PDFs as was the case with the PDFs describing the magnitude of $q_{e,m}$, arising from non-symmetrical phase shifts seen by the 1st and Mth channel. This time, however, the shift of the mean is of different sign: positive for the 1st and negative for the Mth channel. Regardless of means being shifted, standard deviations of the corresponding quasi-Gaussian PDFs remain similar as for the inner channels ($m = 2$ and $m = 3$).

Finally, in Fig. 3(e), (f), we observe the algebraic magnitude of the absolute error between the experimental and the targeted transfer matrix elements, $\mathrm{sign}(\mathfrak{Re}\{\Delta q_m\})|\Delta q_m|$. The effect of mean drifting for edge channels, observed in Fig. 3(a), (b), can now be quantified and, for all analyzed cases stays below $|\Delta q_m| < 0.06$ which yields the maximum relative error of the order of 4% for edge channels. In case of inner channels, the error is centered in the proximity of 0 and, for a given $\Delta\lambda_1$ and R_{AWG} stays below 2% in $> 90\%$ of analyzed random sets.

We extend our analysis to all multichannel modes of PPNN operation according to Fig. 2(a) for $\Delta\lambda_1$ from 0.4 to 1.6 nm (translating to grid spacing of 50 to 200 GHz) and R_{AWG} from -40 to -5 dB, accounting for $M = 8$ channels centered at $c = 4$ when a single modulator for all channels is used, and at m otherwise, aiming to determine the influence of various system parameters on the relative error of the matrix element, δq_m. Figure 4 shows mean values of relative errors over the collection of 10^4 analyzed samples, together with 5% to 95% confidence bounds versus $\Delta\lambda_1$ for AWG crosstalk of -15 dB and versus R_{AWG} for channel spacing of 0.8 nm. As observed in scatter plots given in Fig. 3, we again confirm based on Fig. 4 that edge channels ($m = 1$ and $m = 8$) introduce similar amount of error (lines are overlapping), which is greater than the error encountered by
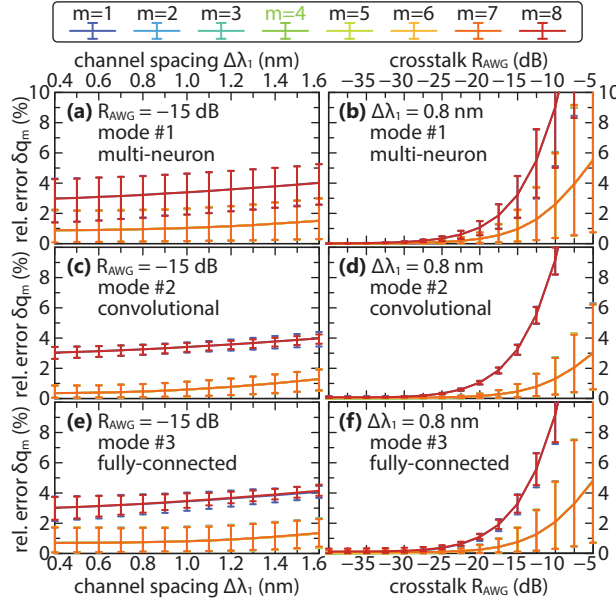
Figure 4. Mean relative errors of the matrix element δq_m (given in percent) with 5% to 95% confidence bounds for (a), (b) multi-neuron, (c), (d) convolutional, and (e), (f) FC mode of operation, depending on (a), (c), (e) channel spacing for $R_{AWG} = -15\,\text{dB}$ and (b), (d), (f) AWG crosstalk for $\Delta\lambda_1 = 0.8\,\text{nm}$.

inner channels ($2 \leq m \leq 7$), also overlapping among themselves. The underlying cause is related to the asymmetry in the filed magnitude and phase shifts accumulated by edge channels when passing through AWG, as previously elaborated. The important conclusion stemming from this overlap is that the number of employed channels M does not pose a challenge for any of the PPNN modes of operation, as long as phase compensation is done within the bias branch following equation (11).

Comparing different modes of operation in Fig. 4 reveals that the mean relative error, be it higher for the edge channels or lower for the inner ones, remains fairly similar for different modes of operation (excluding very high R_{AWG}), having weaker dependence on $\Delta\lambda_1$ than on R_{AWG}. For $R_{AWG} = -15\,\text{dB}$ it does not exceed 4% for any analyzed $\Delta\lambda_1$, however, as the crosstalk increases, the mean error shoots up exponentially, surpassing 10% for the edge channels at $R_{AWG} = -10\,\text{dB}$ and remaining within manageable values of up to 6% for the inner ones even at $R_{AWG} = -5\,\text{dB}$. On the other hand, there is a significant difference in the confidence interval between the modes of operation: it is widest for the multi-neuron mode of operation, given in Fig. 4(a), (b), and reduces for convolutional and FC modes, given in Fig. 4(c)-(f), implying that, although not common, large errors can occur in multi-neuron case. Same evolution of the confidence interval can be seen with respect to AWG crosstalk, Fig. 4(b), (d), (f), revealing that having more DE/MUX stages in mode #1 comparing to the remaining 2 modes of operation is actually responsible for its sizeable spread of errors, as is expected based on the equation (10).

Looking at convolutional, Fig. 4 (c), (d), and FC mode of operation, Fig. 4 (e), (f), difference can be observed in the confidence intervals, and to a certain extent in the mean relative error for the inner channels, indicating that convolutional mode of operation seems to exhibit better overall performance. Yet, from architectural point of view, Figs. 1 and 2, the two are nearly interchangeable. At the same time, our analysis shows that the normalized modulator lengths p_x, q_x, p_w and p_s play marginal role in relative error means and confidence intervals, as was expected having in mind that the accumulated phase given by equations (5b) and (9b) is compensated by the PSs within the bias modulator bank following equation (11). The difference, thus, comes in response to different domains of inputs and weights, i.e., the the quantities enforced jointly to all-channels and the ones enforced on per-channel bases. Repeating the analysis from Fig. 4 for weights restricted to the same domain as inputs, namely $w_{n,m} \in [0,1]$, confirms that the confidence intervals slightly reduce for both modes of operation and, more importantly, become similar in magnitude. This can be explained by reducing the magnitude of crosstalk in weight modulator bank in the FC mode of operation by halving the range of the values $w_{n,m\pm1}$ can take in the equivalent of equation (10) for $w_{n,m}^{AWG}$.

The study of the PPNN performance on fan-in N reveals that the mean relative errors remain similar to the ones in Fig. 4 across different N values, implying that, similar to other analyzed parameters, the number of axons does not pose a challenge to PPNN operation. This indicates that PPNN architecture can be reliably extended into a two-dimensional arrangement, similar to our recently proposed photonic crossbar,[27], yielding K spatially separated neuron outputs. Boosted by WDM, crossbar could support a total of $K \times M$ logical outputs, while also offering flexibility to switch between the different modes of operation, approaching to the photonic FPGA concept.

Conclusion

In this manuscript we present an *in-situ* reconfigurable coherent PNN, exploiting the wavelength domain for achieving parallel operation of multiple neurons with flexible, user-defined interconnection graph, supporting four distinct modes of operation, among others convolutional and fully-connected layer. We carry out a detailed analytical study of the modulator and DE/MUX wavelength dependence, offering a simple approach for restoring the PNN fidelity through phase alignment of the bias signal, revealing that the majority of the residual errors comes from the crosstalk in DE/MUX stages. The analytical approach is benchmarked against Monte-Carlo simulation showing that the residual relative error typically remains within the manageable 2% range for AWG crosstalk of up to $-20\,\mathrm{dB}$. More importantly, the PNN performance does not degrade with the increase of number of channels or the neuron fan-in as long as phase alignment in the bias branch is carried out, supporting seamless network upscaling, including the extension to multi-column arrangements for vector-by-matrix multiplication. The relative error dependence on channel spacing is weak, allowing the PNN to be operated equally well in coarse and dense WDM systems.

Data Availability

The datasets generated during and/or analysed during the current study are available from the corresponding author on reasonable request.

References

1. Kitayama, K.-i. *et al.* Novel frontier of photonics for data processing—photonic accelerator. *APL Photonics* **4**, 090901, DOI: 10.1063/1.5108912 (2019).

2. De Marinis, L., Cococcioni, M., Castoldi, P. & Andriolli, N. Photonic neural networks: A survey. *IEEE Access* **7**, 175827–175841, DOI: 10.1109/ACCESS.2019.2957245 (2019).

3. Shastri, B. J. *et al.* Photonics for artificial intelligence and neuromorphic computing. *Nat. Photonics* **15**, 102–114, DOI: 10.1038/s41566-020-00754-y (2021).

4. Feldmann, J. *et al.* Parallel convolutional processing using an integrated photonic tensor core. *Nature* **589**, 52–58, DOI: 10.1038/s41586-020-03070-1 (2021).

5. Porte, X. *et al.* A complete, parallel and autonomous photonic neural network in a semiconductor multimode laser. *J. Physics: Photonics* **3**, 024017, DOI: 10.1088/2515-7647/abf6bd (2021).

6. Totović, A. R., Dabos, G., Passalis, N., Tefas, A. & Pleros, N. Femtojoule per MAC neuromorphic photonics: An energy and technology roadmap. *IEEE J. Sel. Top. Quantum Electron.* **26**, 1–15, DOI: 10.1109/JSTQE.2020.2975579 (2020).

7. Nahmias, M. A. *et al.* Photonic multiply-accumulate operations for neural networks. *IEEE J. Sel. Top. Quantum Electron.* **26**, 1–18, DOI: 10.1109/JSTQE.2019.2941485 (2020).

8. Miscuglio, M. & Sorger, V. J. Photonic tensor cores for machine learning. *Appl. Phys. Rev.* **7**, 031404, DOI: 10.1063/5.0001942 (2020). https://doi.org/10.1063/5.0001942.

9. Zhang, H. *et al.* An optical neural chip for implementing complex-valued neural network. *Nat. Commun.* **12**, 457, DOI: 10.1038/s41467-020-20719-7 (2021).

10. Shen, Y. *et al.* Deep learning with coherent nanophotonic circuits. *Nat. Photonics* **11**, 441–446, DOI: 10.1038/nphoton.2017.93 (2017).

11. Gu, J. *et al.* Recent advances in convolutional neural networks. *Pattern Recognit.* **77**, 354–377, DOI: https://doi.org/10.1016/j.patcog.2017.10.013 (2018).

12. Leijnen, S. & Veen, F. v. The neural network zoo. *Proceedings* **47**, DOI: 10.3390/proceedings2020047009 (2020).

13. Shawahna, A., Sait, S. M. & El-Maleh, A. FPGA-based accelerators of deep learning networks for learning and classification: A review. *IEEE Access* **7**, 7823–7859, DOI: 10.1109/ACCESS.2018.2890150 (2019).

14. Bogaerts, W. *et al.* Programmable photonic circuits. *Nature* **586**, 207–216, DOI: 10.1038/s41586-020-2764-0 (2020).

15. Pai, S. *et al.* Parallel programming of an arbitrary feedforward photonic network. *IEEE J. Sel. Top. Quantum Electron.* **26**, 1–13, DOI: 10.1109/JSTQE.2020.2997849 (2020).

16. Huang, C. *et al.* On-chip programmable nonlinear optical signal processor and its applications. *IEEE J. Sel. Top. Quantum Electron.* **27**, 1–11, DOI: 10.1109/JSTQE.2020.2998073 (2021).

17. Bogaerts, W. & Rahim, A. Programmable photonics: An opportunity for an accessible large-volume PIC ecosystem. *IEEE J. Sel. Top. Quantum Electron.* **26**, 1–17, DOI: 10.1109/JSTQE.2020.2982980 (2020).

18. Fard, M. M. P. *et al.* Experimental realization of arbitrary activation functions for optical neural networks. *Opt. Express* **28**, 12138–12148, DOI: 10.1364/OE.391473 (2020).

19. Crnjanski, J., Krstić, M., Totović, A., Pleros, N. & Gvozdić, D. Adaptive sigmoid-like and PReLU activation functions for all-optical perceptron. *Opt. Lett.* **46**, 2003–2006, DOI: 10.1364/OL.422930 (2021).

20. Xu, X. *et al.* 11 tops photonic convolutional accelerator for optical neural networks. *Nature* **589**, 44–51, DOI: 10.1038/s41586-020-03063-0 (2021).

21. Mourgias-Alexandris, G. *et al.* Neuromorphic photonics with coherent linear neurons using dual-IQ modulation cells. *J. Light. Technol.* **38**, 811–819, DOI: 10.1109/JLT.2019.2949133 (2020).

22. Mourgias-Alexandris, G. *et al.* A silicon photonic coherent neuron with 10 GMAC/sec processing line-rate. In *Proc. Optical Fiber Communication Conference (OFC) 2021.*, Tu5H.1 (Virtual Conference, 2021).

23. Giamougiannis, G. *et al.* Silicon-integrated coherent neurons with 32 GMAC/sec/axon compute line-rates using EAM-based input and weighting cells. In *Proc. European Conference on Optical Communication (ECOC) 2021.* (Bordeaux, France, 2021).

24. Passalis, N. *et al.* Training noise-resilient recurrent photonic networks for financial time series analysis. In *2020 28th European Signal Processing Conference (EUSIPCO)*, 1556–1560, DOI: 10.23919/Eusipco47968.2020.9287649 (2021).

25. Takahashi, H., Oda, K., Toba, H. & Inoue, Y. Transmission characteristics of arrayed waveguide N × N wavelength multiplexer. *J. Light. Technol.* **13**, 447–455, DOI: 10.1109/50.372441 (1995).

26. Li, H. H. Refractive index of silicon and germanium and its wavelength and temperature derivatives. *J. Phys. Chem. Ref. Data* **9**, 561–658, DOI: 10.1063/1.555624 (1980).

27. Giamougiannis, G. *et al.* Coherent photonic crossbar as a universal linear operator. *Laser & Photonics Rev.* (2021). Submitted for publication.

Acknowledgements

Author contributions statement

All authors conceived the idea and designed the workflow. A.T., G.G., A.T. and N.P. carried out the theoretical and numerical study. All authors analysed and interpreted the results and wrote and reviewed the manuscript.

Additional information

Competing interests The authors declare no competing interests.